RSC Advances

PAPER

View Article Online
View Journal | View Issue

Cite this: *RSC Adv.*, 2022, **12**, 10815

Mixed metal node effect in zeolitic imidazolate frameworks†

Rasmus S. K. Madsen, ‡[a] Malwina Stepniewska,‡[a] Yongjian Yang,‡[b] Ang Qiao,[c] Wessel M. W. Winters,[a] Chao Zhou,[a] Jakob König,[d] John C. Mauro*[b] and Yuanzheng Yue *[a]

We synthesized two series of bimetallic (zinc and cobalt) zeolitic imidazolate frameworks (ZIF-62) under different solvothermal conditions. It is found that the structure of the derived ZIF crystals is highly sensitive to synthesis conditions. One series possesses the standard ZIF-62 structure, whereas the other has a mixed structure composed of both the standard structure and an unknown one. The standard series exhibits a slight negative deviation from linearity of melting temperature (T_m) and glass transition temperature (T_g) with the substitution of Co for Zn. In contrast, the new series displays a stronger negative deviation. These negative deviations from linearity indicate the mixed metal node effect in bimetallic ZIF-62 due to the structural mismatch between Co^{2+} and Zn^{2+} and to the difference in their electronic configurations. The new series involves both cobalt-rich and zinc-rich phases, whereas the standard one shows one homogeneous phase. Density functional theory calculations predict that the substitution of Co for Zn increases the bulk modulus of the ZIF crystals. This work indicates that the structure, melting behaviour, and mechanical properties of ZIFs can be tuned by metal node substitution and by varying the synthetic conditions. Both series of ZIFs have higher glass forming abilities due to their higher T_g/T_m ratios (0.77–0.84) compared to most good glass formers.

Received 3rd February 2022
Accepted 26th March 2022

DOI: 10.1039/d2ra00744d

rsc.li/rsc-advances

Introduction

Metal–organic frameworks (MOFs) are a class of compounds consisting of metal nodes interconnected by organic ligands to form a 2D or 3D porous structure.[1–4] MOFs have received intense interest from chemists and materials scientists since their tunable composition and structure enable potential applications such as catalysis, gas storage, gas separation, and sensors.[5,6] Conventional synthesis approaches of MOFs enabled the formation of fine crystalline powders with the fabrication of large monolithic pieces that were difficult to be obtained.[7] The fine powder of MOFs results in interface interactions and grain boundaries, which are two major engineering challenges in gas or liquid separation.[8–10] It is known that some zeolitic imidazolate frameworks (ZIFs) (a subset of MOFs), which contain imidazole-based ligands that coordinate tetrahedrally to metal ions, forming zeolite crystal topologies, can be melted and then quenched to bulk glass.[2,11–13] MOF glasses are a new family of melt-quenched glasses, which differ from other families such as inorganic, organic, and metallic glasses in terms of chemical bonds, chemical composition, and topological structure. MOF glasses have shown a range of superior properties, *e.g.*, ZIF-62 (Zn Im_{2-x} bIm_x, Im: imidazolate; bIm: benzimidazolate) possesses an ultrahigh glass forming ability (T_g/T_m > 0.84, where T_g is the glass transition temperature, and T_m is the melting point), and high resistance to crystallisation[12]. While other ZIF glasses like ZIF-76 (Zn Im_{2-x} 5-$CbIm_x$, 5-CbIm: 5-chlorobenzimidazole) high porosity.[13] Solid-state ^{67}Zn nuclear magnetic resonance (NMR) spectroscopy revealed that the melting and glass formation of ZIFs led to a high degree of structural disorder.[14] Wang *et al.*[8] recently developed the first glassy MOF membrane, in which ZIF-62 glass was used as the active membrane material on an alumina support. Bulk ZIF-62 glass shows high light transmittance (90%) in the visible range,[15] and possesses anomalous mechanical properties.[16,17] Henke *et al.*[18] revealed that substituting cobalt for zinc in ZIF-62 results in a meltable Co-ZIF-62 phase of the same space group as conventional ZIF-62, *i.e.*, *Pbca*. Bimetallic ZIFs could be produced by introducing two types of metal nodes.[19–21] Most research has focused on bimetallic ZIF-8/ZIF-67 [Zn/Co_1 $MeIm_2$], (MeIm = 2-methyl imidazole), within the realm of

[a]*Department of Chemistry and Bioscience, Aalborg University, Aalborg, DK9220, Denmark. E-mail: yy@bio.aau.dk*

[b]*Department of Materials Science and Engineering, The Pennsylvania State University, USA. E-mail: jcm426@psu.edu*

[c]*Wuhan University of Technology, Wuhan, 430070, China*

[d]*Advanced Materials Department, Jožef Stefan Institute, Ljubljana, 1000, Slovenia*

† Electronic supplementary information (ESI) available: Optical images, SEM images, EDX elemental mapping, XRD patterns, ^{1}H-NMR spectra, ATR FT-IR spectra, ICP-OES ratio, DSC scans, TGA data, and DTA-MS analysis. See DOI: 10.1039/d2ra00744d

‡ These authors equally contributed to this work.

catalysis.[19–21] A recent study by Bumstead *et al.*[22] investigated the effect of structural disorder within a ZIF-62-type network. They found that the T_m decreased as they introduced cobalt into the zinc network. Zn/Co-ZIF-62 exhibits super-broadband mid-infrared (Mid-IR) luminescence,[23] which is important for photonic applications. Recently, the computational modelling of ZIFs (and MOFs)[24,25] through density functional theory (DFT)[26–29] and molecular modelling[30–36] has been performed to understand the effect of both nodes and linkers[37] on the ZIF structure.

In this work, we report a systematic study on the effect of metal substitution on thermodynamic, kinetic, and mechanical properties in Co/Zn-ZIF-62 series. Two series of Co/Zn ZIF crystals were synthesized *via* a solvothermal method. The first series was Co/Zn-ZIF-62 (*Pbca* space group) based on the work of Henke *et al.*[18] The second series was synthesized by the experimental procedures described elsewhere,[17] which is a biphasic Co/Zn-ZIF-new series, *i.e.*, a series containing both a Zn-rich phase and a Co-rich phase. The two series of crystals were structurally characterized through powder X-ray diffraction (PXRD), scanning electron microscopy (SEM), as well as energy-dispersive X-ray spectroscopy (EDX), and chemically *via* ^{1}H solution nuclear magnetic resonance (S-NMR). The Co/Zn-ZIF-62 series showed structural features similar to those known in the literature, whereas the Co/Zn-ZIF-new series featured both a different crystal structure and an unexpected molecular structure of the organic ligands. The Co/Zn-ZIF-new series was also analyzed *via* infrared spectroscopy (FT-IR) and inductively coupled plasma optical emission spectroscopy (ICP-OES) to investigate the nature of its structure. Both series were analyzed *via* differential scanning calorimetry (DSC) to investigate how T_m and T_g vary with the substitution of Co for Zn. In this work, we also conducted DFT and classical force field (FF) calculations on the crystalline phase of the bimetallic ZIF-62 systems, in order to predict the change in mechanical properties of the crystals, and how bond lengths and bond strength increase when substituting cobalt for zinc.

Experimental

Synthesis of ZIF crystals

Standard Co/Zn ZIF-62 synthesis. Solvothermal synthesis of Co/Zn-ZIF-62 was carried out in accordance with Table 1 and based on a method reported by Henke *et al.*[18] For brevity, the samples are named according to the reaction fraction of cobalt, *e.g.*, a reaction batch of $Zn_{0.9}Co_{0.1}$-ZIF-62 is called 0.1-ZIF-62. The stock solutions for synthesis contain 0.14 M zinc nitrate hexahydrate ($Zn(NO_3)_2\cdot 6H_2O$), 0.14 M cobalt nitrate hexahydrate ($Co(NO_3)_2\cdot 6H_2O$), 0.40 M imidazole ($C_3H_4N_2$, Im), 0.06 M benzimidazole ($C_7H_6N_2$, bIm), and *N*,*N*-dimethylformamide (DMF). The volume of each reactant for each sample is given in Table 1. The solutions were mixed by stirring for 30 minutes, and then they were transferred to a 100 mL Teflon-lined steel autoclave and placed in an oven at 130 °C for 168 hours. The oven was turned off, and the autoclaves were cooled under ambient pressure overnight to room temperature. The crystals were collected from the autoclave and washed three times with DMF. The samples were centrifuged at 4500 rpm for 5 minutes between each wash. After the last wash, the samples were dried overnight at 110 °C.

Table 1 Volume concentration of the stock solutions used to synthesize bimetallic ZIF-62 samples

Sample	0.14 M $Zn(NO_3)_2\cdot 6H_2O$ (mL)	0.14 M $Co(NO_3)_2\cdot 6H_2O$ (mL)	0.40 M Im (mL)	0.06 M bIm (mL)
0.0-ZIF-62	25	—	25	25
0.1-ZIF-62	22.5	2.5	25	25
0.2-ZIF-62	20	5	25	25
0.4-ZIF-62	15	10	25	25
0.6-ZIF-62	10	15	25	25
0.8-ZIF-62	5	20	25	25
0.9-ZIF-62	2.5	22.5	25	25
1.0-ZIF-62	—	25	25	25

Biphasic Co/Zn-ZIF-new synthesis. A different synthesis route was used to synthesize the biphasic Co/Zn-ZIF-new series. Zinc nitrate hexahydrate, cobalt nitrate hexahydrate, imidazole, benzimidazole, and DMF solvent were used, as shown in Table 2. The solutions were mixed for 30 minutes, transferred to the same type of autoclaves as used for the synthesis of Co/Zn-ZIF-62, and heated at 120 °C for 48 hours, in contrast to 130 °C and 168 hours in the standard synthesis. The recovered crystals were washed three times with DMF and centrifuged at 4500 rpm for 5 minutes between each wash, followed by drying at 110 °C overnight. These samples are also named according to the ratio of cobalt content to the total metal content, *i.e.*, $Zn_{0.9}Co_{0.1}$-ZIF-new is called 0.1-ZIF-new, where 'new' refers to the change in structure compared to the standard ZIF-62.

Structural analysis

A PANalytical Empyrean equipped with a Cu X-ray source (λ = 1.54098 Å) was used to collect powder X-ray diffraction (PXRD) patterns. The crystalline powders were loaded onto an amorphous silicon sample holder (PANalytical) and measured using a Ni-filter, 0.04 rad soller, 1/8° divergence slit, and 1/4° anti-scatter slit on the incident side and a 7.5 mm anti-scatter slit and a 0.04 rad soller on the diffracted side. The diffraction spectra were collected with $2\theta = [5.009583°, 79.995010°]$ using a step-size of 0.006565°. The samples were dried at 350 °C in an argon atmosphere before the measurements.

Solution ^{1}H-NMR (Bruker Avance III 600 MHz spectrometer) was used to determine the composition of organic linkers in each crystalline sample. All samples were digested using 200 μL of a 1 : 5 DCl (35% conc., 99% 2H, Aldrich) : dimethyl sulfoxide (DMSO) (VWR, 99.80% 2H) solution. The pulse sequence used was a 1D experiment with composite pulses.[38] A 5 seconds continuous-wave irradiation of $\gamma B_1/2\pi = 50$ Hz was used to suppress the water signal. The total recycle delay was 28 s. A Zeiss 1540 XB was used to perform both scanning electron microscopy (SEM) and energy-dispersive X-ray spectroscopy (EDX) to characterise the crystalline samples. EDX data acquisition and analysis were performed using the NSS3 X-ray microanalysis software

Table 2 Volume concentration of the stock solutions used for the biphasic Co/Zn-ZIF-new synthesis

Sample	0.6 M $Zn(NO_3)_2 \cdot 6H_2O$ (mL)	0.6 M $Co(NO_3)_2 \cdot 6H_2O$ (mL)	4 M Im (mL)	0.5 M bIm (mL)	DMF (mL)
0.0-ZIF-new	17.45	—	33.82	21.82	1.91
0.1-ZIF-new	15.71	1.75	33.82	21.82	1.91
0.2-ZIF-new	13.96	3.49	33.82	21.82	1.91
0.4-ZIF-new	10.47	6.98	33.82	21.82	1.91
0.6-ZIF-new	6.98	10.47	33.82	21.82	1.91
0.8-ZIF-new	3.49	13.96	33.82	21.82	1.91
1.0-ZIF-new	—	17.45	33.82	21.82	1.91

(Thermo Fischer Scientific Inc.). The accelerating voltage of the electron beam is 10 kV. Fourier-transform infrared spectroscopy (FT-IR) measurements were performed on Co/Zn-ZIF-new samples in a wavenumber range 4000–400 cm^{-1} in absorbance mode using Bruker Tensor II equipped with platinum attenuated total reflectance (ATR).

Thermal analysis

The melting, glass transition, and mass change of the samples were studied using a Netzsch STA 449 F1 instrument that combines differential scanning calorimetry (DSC) and thermal gravimetric analysis (TGA). The samples were placed in a platinum crucible situated on a sample holder of the STA at room temperature. The samples were held for 5 min at an initial temperature of 343 K, then heated at 10 K min^{-1} to 733 K, and then cooled back to 393 K at 10 K min^{-1}, thus forming the standard glass. Subsequently, the second upscan was conducted from 393 K to 643 K at 10 K min^{-1}. To determine the isobaric heat capacity of the samples, both the baseline (blank) and the reference sample (sapphire) were measured.

In order to identify the decomposition gases, additional TGA were performed using a Jupiter 449 simultaneous thermal analysis (STA) instrument coupled with a 403 C Aëolos mass spectrometer (MS) (Netzch, Selb, Germany). The measurements were performed with a heating rate of 10 K min^{-1} in an argon atmosphere. A small amount of powder (11–14 mg) was inserted into an uncovered alumina crucible. The ionised species of the gases released from the heat-treated sample were detected by the MS and compared to the gas ionic spectra data from the NIST Standard Reference Database.[58]

Simulations of ZIF-62 based samples

The atomic configuration for crystalline Zn-ZIF-62 was obtained from the Cambridge Structural Database (CSD, CCDC number 671070). The original structure does not contain cobalt atoms. To create $Zn_{(1-x)}Co_x$-ZIF-62, an increasing number of zinc atoms were substituted by cobalt atoms. Because the distance between the nodes (zinc and cobalt atoms) in ZIF-62 is relatively large (>6 Å) with direct substitution of zinc atoms with cobalt atoms, the interaction between the cobalt sites can be ignored. Both the DFT calculation and the force field calculation were attempted. While the DFT calculation gives more accurate results, the force field calculation is much faster because it uses a classical force field and requires less computational resources.

For the DFT calculation, the crystal Zn-ZIF-62 structure was relaxed using the projector augmented-wave PAW method as implemented in the Vienna *ab initio* simulation package (VASP). An energy cut-off of 650 eV was applied for the plane-wave basis set. Perdew–Burke–Ernzerhof (PBE) functional was used to evaluate the electronic exchange and correlation with a D3 van der Waals correction by Grimme.[39] The Brillouin zone was sampled at the Γ-point, which is considered sufficient for the ZIF-62 unit cell dimension of 296 atoms. For the structural relaxation, we set the EDIFF to be 10^{-3}–10^{-4} eV. The ionic relaxation stops when all forces are converged to less than 0.005 eV $Å^{-1}$. In order to calculate the bulk modulus, the ZIF-62 structures of different Co concentrations had been relaxed with a series of volume changes from −4% to 2%. The Birch–Murnaghan equation of state[40] was used to extract the bulk modulus from the energy curve at different volumes.

In the classical FF calculations, the bimetallic $Zn_{(1-x)}Co_x$-ZIF-62 structures from the above DFT calculations are first subjected to energy minimisation using the conjugate gradient algorithm as implemented in LAMMPS41 (ref. 41) with an energy tolerance the force tolerance of 4.3×10^{-17} eV and 7×10^{-16} nN, respectively, for the minimisation. For the interactions between atoms, the classical Universal Force Field for Metal–Organic Frameworks (UFF4MOF) force field[42,43] is used. UFF4MOF is based on the universal force field[44] and has been extended for MOF chemistries. UFF4MOF contains transition metals, including zinc and cobalt, which are commonly found in ZIFs. It has been shown that the UFF4MOF force field can accurately reproduce the structural characteristics and the bulk modulus for many different types of MOFs that have been verified experimentally.[31,43,45] To calculate the bulk modulus, the ZIF-62 structure is relaxed with a series of volume changes from −3% to 3% around the equilibrium volume. The bulk modulus is obtained by fitting the equation of state using the Birch–Murnaghan equation.[40]

To calculate the Young's modulus, the ZIF-62 sample is stretched or compressed in one Cartesian direction up to ~5%, while the external pressure in the two other Cartesian directions is kept around zero. The Young's modulus at 0 K is extracted from the stress–strain curve.

Results and discussion

Modelling and characterisation of standard Co/Zn-ZIF-62

DFT and classical FF calculations were carried out using the Zn-ZIF-62 structure as an initial configuration. Fig. 1 shows the FF results for Zn-ZIF-62, *viz.*, the unit cell volume, bulk modulus, and Young's modulus. Densities of crystalline Zn-ZIF-62 phase determined from DFT and FF methods are close to the published density data[46] and the values obtained from the present experiment (Table S1†). As shown in Fig. 1b, the unit cell volumes from both DFT and FF calculations differ by ~0.5%, and the volume of the cobalt substituted sample decreases up to 1% when the substitution of cobalt for zinc atoms reaches 62.5%. This decrease can be partially attributed to the shorter Co–N bond compared to Zn–N bond according to the DFT calculation by Krokidas *et al.*[19,47] The decrease in bond length is hypothesised to stem from the different electronic configurations of the metal ions ($3d^{10}$ for Zn^{2+} and $3d^{7}$ for Co^{2+}). The unfilled $3d^{7}$ orbital is able to interact with electrons from the imidazolate linkers, which strengthens the interaction between cobalt and the linkers, resulting in the decrease in bond length. It has been experimentally observed that cobalt ZIFs have a smaller unit cell volume than their zinc counterparts.[48]

For the powder samples (see Fig. S1†), the crystals are too small to measure the mechanical properties experimentally, and thus, only theoretical determination of bulk modulus and Young's modulus is reported here to show the effect of substitution of cobalt for zinc on the Zn-ZIF-62 structure. The bulk and uniaxial Young's moduli of the crystalline ZIF-62 are shown in Fig. 1c DFT and FF calculations yield an average bulk modulus of 3.8 ± 0.2 GPa and 4.7 ± 0.2 GPa for all samples. With increasing cobalt content, there is a moderate increase in the bulk modulus. The Young's modulus has a different trend with increasing substitution, depending on the crystal orientation, *i.e.*, it increases in the [100] direction, decreases in the [001] direction, and remains roughly the same in the [010] direction. The finding that the unit cell volume decreases with increasing cobalt content agrees well with the finding of bulk modulus slightly increasing, as it has been found previously in the literature that the bond length is inversely proportional to the bulk modulus.[49,50]

The computational results predict that both zinc and cobalt ions are compatible with the ZIF-62 crystal structure. The random substitution of zinc ions with cobalt ions in the cag topology does not negatively impact the calculated mechanical strength of the crystal. Characterisation of the synthesized crystals was performed to confirm that there is no change in the space group, while the bond strength increases slightly, when substituting cobalt for zinc in ZIF-62.

An image of the eight standard Co/Zn-ZIF-62 samples can be seen in Fig. S1,† revealing a color gradient as cobalt is substituted for zinc. The color gradient agrees with the relative cobalt content, as revealed by UV-Vis in Fig. S2.† Fig. 2a presents the XRD patterns of the bimetallic Co/Zn-ZIF-62 crystals synthesized by the standard approach.[18] The patterns of all Co/Zn-ZIF-62 samples agree well with the reference crystallographic information files (CIF) (Cambridge Crystallographic Data Centre (CCDC)[51] (ZIF-62: CCDC number 671070)) used to generate the XRD patterns. The decrease in the signal-to-noise ratio for the samples containing predominantly cobalt is due to the fluorescence caused by cobalt having its X-ray absorption edge close to the energy level of Cu-radiation.[52] Fig. 2b and c confirm that the benzimidazole to imidazole ratio does not change noticeably when substituting cobalt for zinc in the Co/Zn-ZIF-62 samples. Thus, we can infer that the changes in both the mechanical properties (Fig. 1) and the thermal behaviours (shown below) are a consequence of metal substitution. Additionally, SEM and EDX reveal that cobalt is evenly distributed in the crystal of all the Co/Zn-ZIF-62 samples, as seen in Fig. S3–S10.† The shape of the crystals deviates from the octahedral morphology reported in the literature.[8] This deviation can be explained by the removal of DMF from the pores during heat-treatment at 350 °C.

The structural characterisation of the standard series agrees well with the computational results, suggesting that zinc and cobalt ions can co-exist in the same bimetallic crystal structure without phase separation. Based on the computational results shown earlier, as well as previous experimental results for Co-

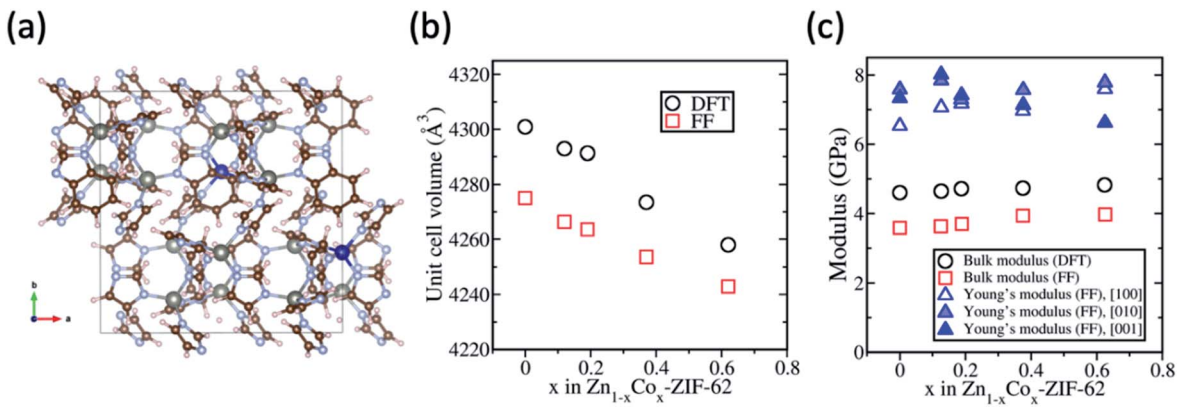

Fig. 1 (a) Crystal structure of $Zn_{1-x}Co_x$-ZIF-62 with $x = 0.125$. The blue atoms are cobalt, and the large grey atoms are zinc. (b) Unit cell volume of crystalline ZIF-62 as a function of increasing substitution with cobalt. (c) Moduli of crystalline ZIF-62 as a function of increasing substitution with cobalt.

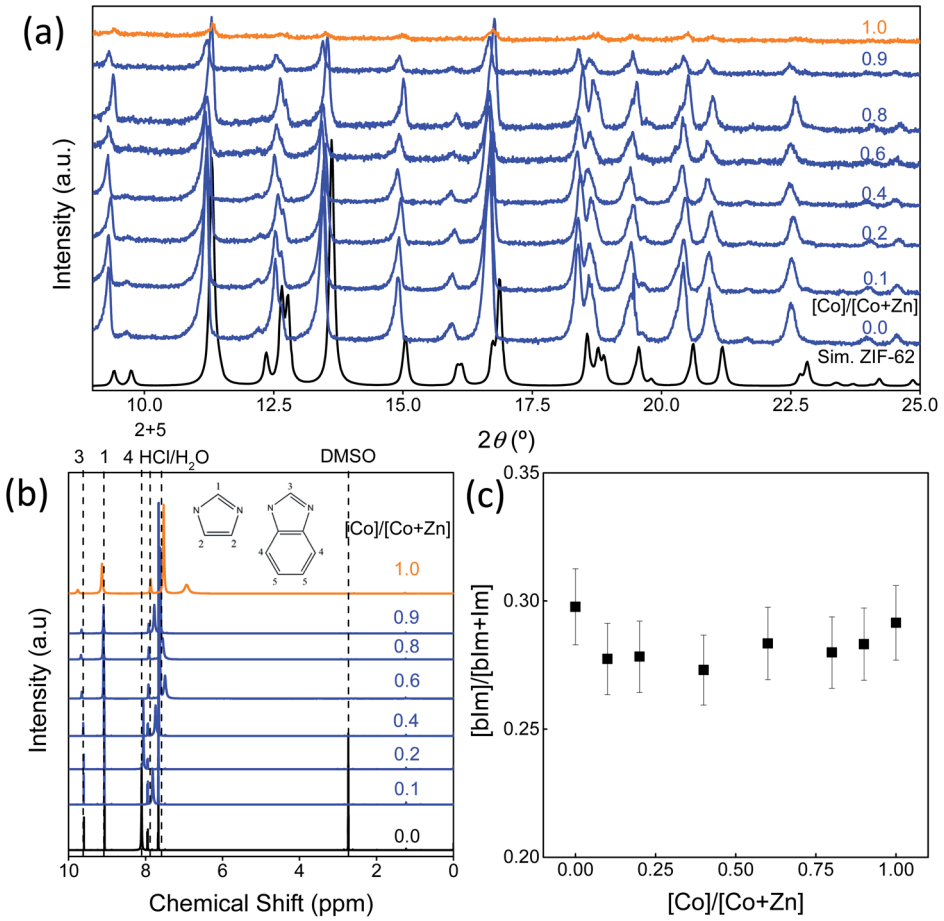

Fig. 2 (a) XRD patterns of the standard ZIF-62 series with varying the ratio of cobalt content to the total metal content ([Co]/([Co + Zn])). (b) Liquid ^{1}H-NMR spectra of Co/Zn-ZIF-62 samples. Dashed lines: the typical peaks associated with imidazole, benzimidazole, and solvents. (c) Fraction of benzimidazole content in the total linker content for each cobalt modified ZIF-62, with a margin of error of 5%.

ZIF-62,[18] it is expected that T_m would linearly increase as cobalt is substituted for zinc in the ZIF-62 crystal structure due to stronger bonding between the cobalt nodes and the linkers. Fig. 3a and b show the thermal responses of the Co/Zn-ZIF-62 samples for the first and second upscans, respectively. The first upscan curve reveals two distinct endothermic responses. The first is attributed to the removal of DMF from the pores, while the second is ascribed to the melting process, with T_m defined as the offset of the melting peak. The second upscan curves in Fig. 3b for all the Co/Zn-ZIF-62 samples show clear glass transition peaks, strongly confirming the glassy nature of melt-quenched samples. Fig. 3c displays the T_m of the standard Co/Zn-ZIF-62 structures, which agrees well with that of the as-synthesized crystals in Henke group's work.[18] T_m is seen to anomalously decrease as cobalt is introduced (0.1-ZIF-62), and then non-linearly increases with a gradual substitution of cobalt for zinc. This effect is rather unexpected, when looking at the simulation work of Fig. 1b and c. Fig. 3d demonstrates that T_g also has a similar drop, followed by an increase as the degree of cobalt substitution increases. Fig. 3c and d shows that both T_m and T_g follow a similar trend when substituting cobalt for zinc. T_m drops slightly from 707 K to 700 K and then non-linearly increases to a maximum of 712 K, slightly higher than reported previously. Similarly, T_g has a small drop from 599 K to 591 K and then increases to 597 K when all zinc nodes are substituted with cobalt. For the standard Co/Zn-ZIF-62 series, there is only one homogeneous crystalline phase, and the minima of both T_m and T_g are found at the composition of Co/(Co + Zn) = ~0.1. The observed minimum in T_m could be a consequence of the mixed metal node effect that has the same fashion as the mixed modifier effect in oxide glasses.[53,54] The mixed modifier effect in oxide glasses refers to a non-additive change of some transport properties when one type of modifier (*e.g.*, sodium ion) is substituted by another (*e.g.*, potassium), *i.e.*, a positive or negative deviation from the linear trend of a property with the modifier substitution.[53,54] In the studied standard Co/Zn-ZIF-62, the partial substitution of cobalt for zinc (and *vice versa*) causes an increase in structural instability, possibly due to structural mismatch effects caused by the difference in bond length and strength between Co–N and Zn–N bonds. This bond difference arises from the difference in electron configurations between the two types of metal ions (d^7 for Co^{2+} and d^{10} for Zn^{2+}). The structural instability enhances the atomic vibrations, and hence, the Lindemann criterion for

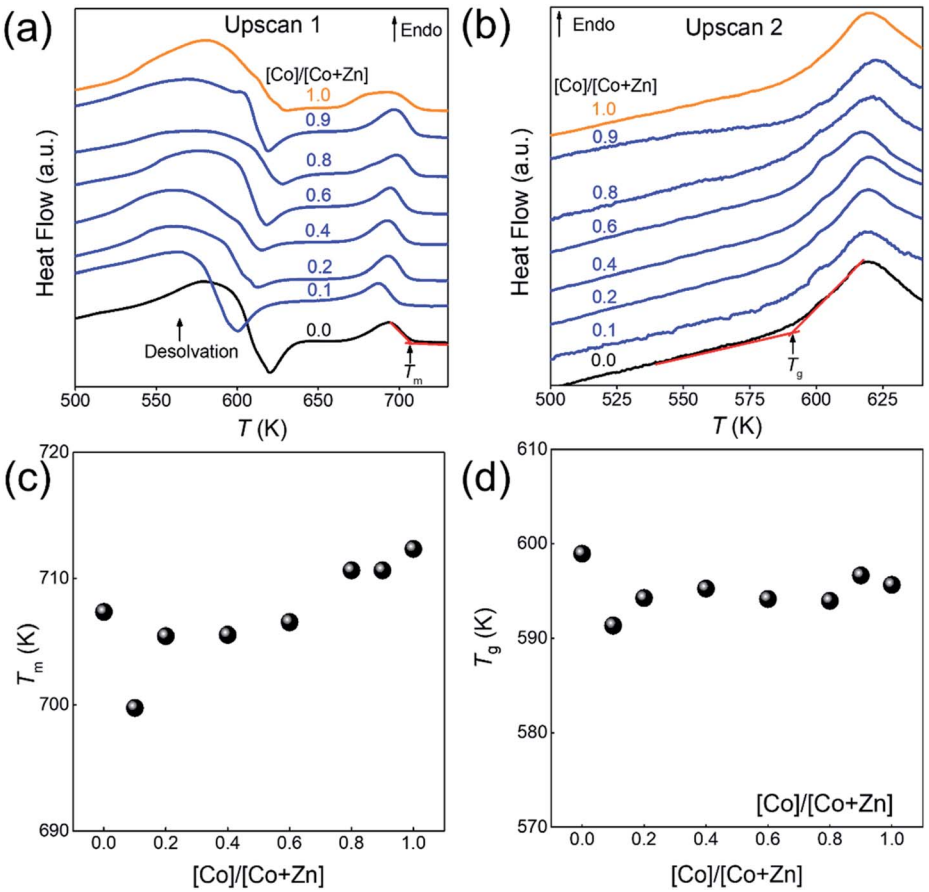

Fig. 3 (a) The first upscan (10 K min^{-1}) shows two endothermic peaks, assigned to desolvation followed by melting. (b) Glass transition behaviour during the second upscan (10 K min^{-1}). (c) T_m of Co/Zn-ZIF-62 with increasing substitution with cobalt. (d) T_g of Co/Zn-ZIF-62 with increasing substitution with cobalt. Inset: T_g/T_m ratio for the same series.

melting would be more easily fulfilled.[55] However, the pure Co-ZIF-62 exhibits higher T_m than its counterpart – pure Zn-ZIF-62. The higher T_m of pure Co-ZIF-62 can be attributed to the stronger interaction between the linkers and cobalt ions, as predicted from the DFT and FF calculations, and also from the experimental data reported by other authors.[18]

Impact of synthesis condition on Co/Zn-ZIF-62 structure

Fig. S11† shows the optical image of the seven ZIF samples. A clear relationship is seen between the intensity of the purple color of the sample and the amount of cobalt added during the synthesis. These samples were analyzed *via* X-ray diffraction to identify the crystal structure (Fig. S12†). When sufficient cobalt nitrate is used in the solvothermal synthesis, an additional phase is observed for the resulting crystals, with the peaks marked with asterisks (*). In Fig. 4a, the diffraction pattern of 1.0-ZIF-new is compared to that of 1.0-ZIF-62. A different XRD pattern is observed, confirming that 1.0-ZIF-new has a different structure from the standard 1.0-ZIF-62. This new type of ZIF crystal shows fewer peaks in the XRD pattern than the standard 1.0-ZIF-62. This suggests that the new structure is likely of higher symmetry than that of the standard sample, as fewer peaks (*i.e.*, fewer unique *d*-spacings) are present. The absence of diffraction peaks at higher angles suggests that the structure is indeed a Co-based metal–organic framework. It is assumed that the formation of this structure is a result of the high reactant concentrations used during the solvothermal synthesis.

S-NMR spectroscopy was employed to verify the presence of the organic linkers in the biphasic frameworks and the differences in linker composition between 1.0-ZIF-62 and 1.0-ZIF-new (Fig. 4b). Fig. S13† plots the NMR spectra, where the signals of 0.0-ZIF-new agree with those of the standard 0.0-ZIF-62 spectra. However, as cobalt nitrate is substituted for zinc nitrate during the synthesis, the imidazole and benzimidazole signals decrease in intensity for the resulting crystals. Two new peaks at ~5.84 and 6.83 ppm (Fig. 4b) appear and increase in intensity with increasing the cobalt nitrate content. It was assumed that the high concentration of nitrate ions in the presence of cobalt would catalyze the nitration of imidazole to 4-nitroimidazole. The NMR spectrum of 4-nitroimidazole, dissolved in the same NMR solvent, can be found in the ESI (Fig. S14†). The spectrum shows no peaks in the 5–7 ppm range, thus excluding the possibility that the emerging signal arises from nitrated imidazole. To determine the distribution of zinc and cobalt in the two crystal phases, SEM and EDX analyses were performed on the 0.6-ZIF-new sample, as seen in Fig. 5. Two crystal particles

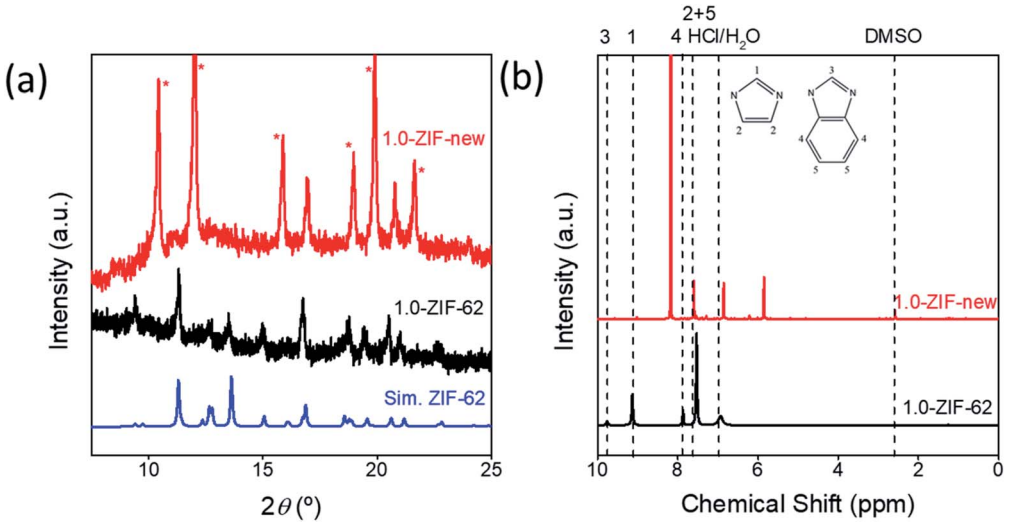

Fig. 4 (a) X-ray diffraction pattern of simulated ZIF-62 (blue), 1.0-ZIF-62 (black), and 1.0-ZIF-new. (*) highlights the new peaks emerging from the new ZIF structure. (b) ^{1}H-NMR of 1.0-ZIF-62 (black) and 1.0-ZIF-new (red). The 1.0-ZIF-new sample clearly shows the disappearance of the hydrogen peaks marked as 1 and 3, while two new peaks appear.

with different morphologies are observed, *i.e.*, octahedral and spherical shapes in column 1 of Fig. 5. The SEM image in Fig. S15a† shows the sample containing only Zn, *i.e.*, 0.0-ZIF-new, which contains crushed ZIF-62 particles, where some of the flat surfaces of the standard ZIF-62 morphology remain. The SEM image in Fig. S15b† illustrates the sample containing only

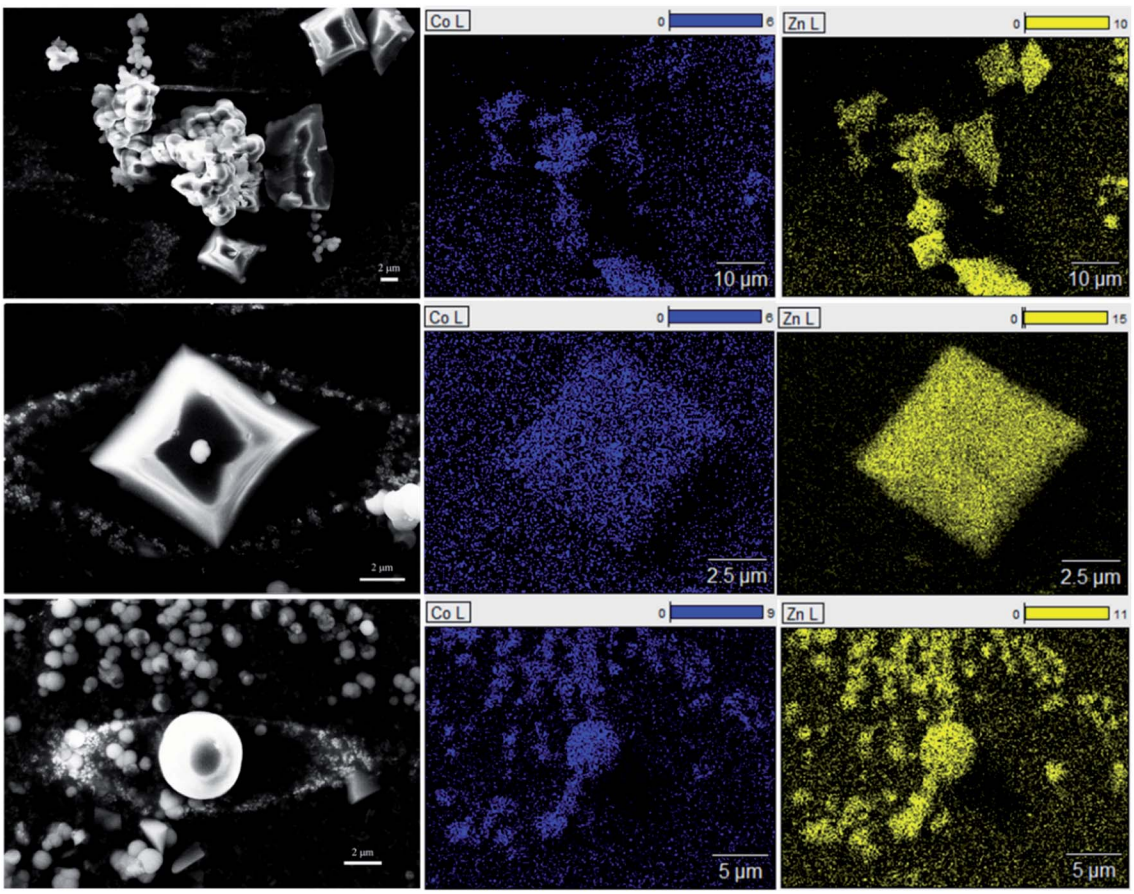

Fig. 5 Left column is the SEM image of the area detected for EDX elemental mapping for cobalt (middle column) and zinc (right column).

Co, *i.e.*, 1.0-ZIF-new, where only spherical particles are present. The SEM images indicate that there is a difference in the crystal morphologies between the standard ZIF-62 structure (*i.e.*, the standard phase) and the new structure (*i.e.*, the new phase). The EDX elemental mapping in Fig. 5 (see columns 2 and 3) reveals that both morphologies contain zinc and cobalt, which confirms that both metal nodes are incorporated into the two crystal structures. EDX elemental analysis in Fig. S16† confirms that the octahedral ZIF-62 crystals contain zinc predominantly, while the new spherical crystal structure contains more cobalt. The metallic heterogeneity in the new series of ZIFs could be ascribed to the preferential incorporation of cobalt into the new phase.

ATR FT-IR was employed to detect the changes of the chemical bonds in the Co/ZIF-new samples (Fig. S17†). Several changes in the signal can be observed. First, the peaks at 1677 and 1384 cm^{-1}, which are assigned to the DMF,[18,56,57] disappear with increasing the cobalt content, being attributed to the new phase with a denser structure. Second, some of the peaks around 1150–1300 cm^{-1} (assigned to C–N and C–C stretching) change in shape as cobalt is substituted for zinc. Simultaneously, the double peak at ~1480 cm^{-1}, which is assigned to aromatic ring stretching, varies in line shape with increasing the cobalt content. The FT-IR results (Fig. S17†) indicate that signals corresponding to imidazole and benzimidazole rings are still present. In combination with the S-NMR findings in Fig. S13,† it is evident that the imidazole and benzimidazole structures have changed, while the exact chemical structure of the linkers remains unknown. It is reasonable to infer that the formation of the unknown linker is caused by cobalt nitrate, and hence, cobalt preferentially stays in the new phase. The absolute Co/(Co + Zn) ratio of these samples was analysed *via* ICP-OES. Fig. S18† reveals that there is a non-linear relationship between the Co/(Co + Zn) ratio used during the synthesis and the ratio detected in the resulting ZIF samples. This is explained by the phase separation exhibited in Fig. S19,† where a portion of the new phase with higher cobalt content could have been lost during the washing and collecting process.

Fig. 6a and b shows the changes of both T_m and T_g values with the substitution of cobalt for zinc for two series of ZIFs. The data points are acquired from the first and second DSC scans shown in Fig. 3a, b and S20.† It is seen in Fig. 6a and b that both T_m and T_g show negative deviations from linearity with substitution of cobalt for zinc, which could be caused by two factors. The first is the mixed metal node effect as the two crystal phases both contain zinc-ions and cobalt-ions. The second is a eutectic effect caused by the presence of two discrete phases resulting in a drop in T_m. Given that 0.1-ZIF-new in Fig. S12† reveals no detectable quantity of the new phase, the mixed metal effect is likely to have a greater effect at lower Co/(Co + Zn) ratios on T_m and T_g. The deviations in both T_m and T_g are much larger for the new ZIF series than that of Co/Zn-ZIF-62. Due to the absence of the new phase at low cobalt content, it is reasonable to infer that the effect on T_m and T_g is initially driven by the mixed metal node effect, but at higher cobalt concentrations, multiple effects *e.g.*, the effect of two discrete phases could cause the changing trend in T_m and T_g. These results imply that the atomic vibration in the new series of ZIF more easily meets Lindemann's criterion for melting. Moreover, it is seen in Fig. S21† that the Co/Zn-ZIF-new series undergoes a noticeable loss of mass during the melting process. The origin of the mass loss is investigated by a thermogravimetric analyzer coupled with mass spectrometry (TGA-MS) (Fig. S22†). The TGA-MS analysis shows that mainly NH_3 and NO gases are released during melting, suggesting that the linkers in the new series are more unstable than those in the standard series. The 0.0-ZIF-new sample has a T_m at 706 K and a T_g at 588 K, which correspond to the values for standard Zn-ZIF-62. 1.0-ZIF-new has a higher T_m at 724 K and a lower T_g at 573 K. The higher T_m might be due to a denser structure, as indicated by the lack of DMF signals from the FT-IR results.

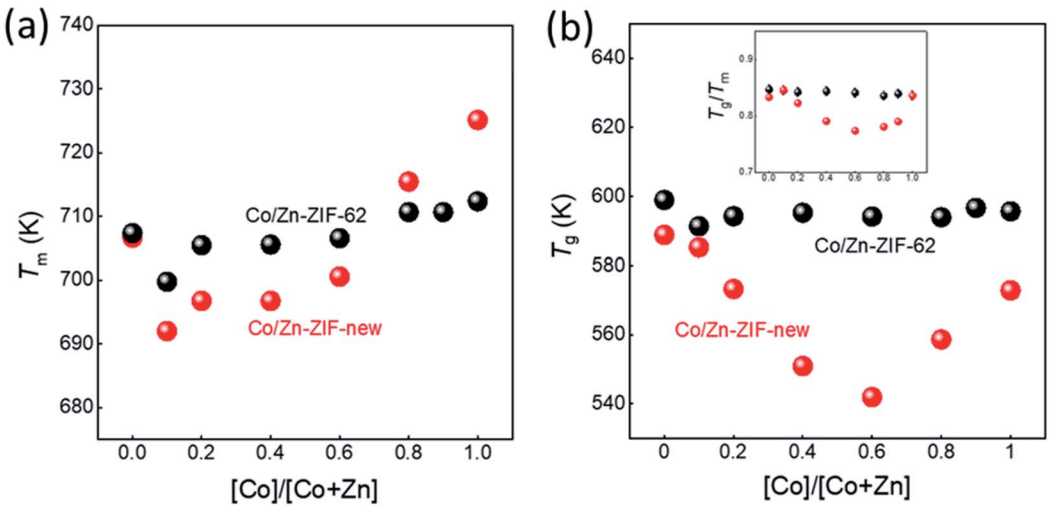

Fig. 6 (a) T_m of Co/Zn-ZIF-62 series (black) and Co/Zn-ZIF-new series (red). (b) T_g of Co/Zn-ZIF-62 series (black) and Co/Zn-ZIF-new series (red). Inset: T_g/T_m ratios for both Co/Zn-ZIF-62 series and Co/Zn-ZIF-new series.

The inset of Fig. 6b shows the dependence of T_g/T_m ratios for the two studied ZIF series on the Co–Zn substitution. As is known, T_g/T_m is a measure of the glass forming ability (GFA) of a glass former, *i.e.*, the higher the T_g/T_m ratio of a glass former is, the higher its GFA is. It is seen that both series show higher GFA since their T_g/T_m ratios (0.77–0.84) are significantly higher than that of most good glass formers ($T_g/T_m = 0.67$).[12] Interestingly, there is no change in T_g/T_m with metal node substitution in the standard series, indicating that the GFA remains the same. However, in contrast to the standard series, the new series exhibits smaller T_g/T_m ratios, suggesting that the GFA of the latter is relatively lower. In addition, the T_g/T_m ratio shows a non-monotonic trend with substituting cobalt for zinc, *i.e.*, there is a minimum T_g/T_m ratio at Co/(Co + Zn) = 0.6. This composition shows a pronounced phase separation, as shown in Fig. 5. This fact agrees with the general notion that a glass former with stronger phase separation tendency features a lower GFA.

Conclusions

We synthesized two series of bimetallic cobalt/zinc zeolitic imidazolate frameworks based on ZIF-62. It was found that the structure of the derived ZIF crystals strongly depended on synthesis conditions. One series of ZIF crystals were obtained by using the standard synthesis condition reported in the literature, which possessed the standard ZIF-62 structure. In contrast, the other series, which was produced at a lower temperature (120 °C) for a shorter duration (48 hours), had a mixed structure composed of both the standard structure and a new one. We predicted the mechanical properties of the standard series of Zn/Co-ZIF-62 through DFT and FF calculations.

An interesting mixed metal node effect was observed in bimetallic ZIF-62 samples, *i.e.*, negative deviations from linearity of T_m and T_g for both series of bimetallic ZIF-62 with substitution of Co for Zn. Notably, the new series displayed a stronger mixed metal node effect at lower Co substitution. This mixed metal node effect was attributed to the structural mismatch between Co^{2+} and Zn^{2+}, and to the difference in their electronic configurations. The network became destabilised by introducing the dissimilar cobalt-ion into the ZIF crystal. Some of the samples in the new series contained both cobalt-rich and zinc-rich phases, whereas the standard one showed only one homogeneous phase. It was found that during melting, the Co/Zn-ZIF-new samples underwent a partial decomposition of an unknown species, suggesting that the new phase had a lower thermal stability than the standard phase. The above findings are instrumental to the understanding of the structure and thermodynamic properties of MOF glasses and to the design of novel MOF glass formers. Concerning the strong mixed metal node effect of the Co/Zn-ZIF-new series, the chemistry and structure of this series should be further investigated to reveal the melting mechanism of MOFs and to design new MOF glass formers.

Both series of ZIFs have higher GFA due to their higher T_g/T_m ratios (0.77–0.84) compared to most of the good glass formers. T_g/T_m remains the same with metal node substitution in the standard series, and hence there is no change in GFA. However, the new series exhibits smaller T_g/T_m ratios, *i.e.*, lower GFA, than the standard series. In addition, the new series shows a minimum T_g/T_m ratio at Co/(Co + Zn) = 0.6.

Conflicts of interest

The authors declare no competing financial interest.

Acknowledgements

The authors thank Villum Fonden (grant no. 13253) for the support. A. Q. acknowledges the National Natural Science Foundation of China (no. 22175135) and the Fundamental Research Funds for the Central Universities (WUT: 2021IVA099, 2021III018JC) for their support. Y. Y. thank the Independent Research Fund Denmark for the support (1026-00318B).

References

1 K. S. Park, Z. Ni, A. P. Cote, J. Y. Choi, F. J. Uribe-Romo, H. K. Chae, M. O'Keeffe and O. Yaghi, *Proc. Natl. Acad. Sci. U. S. A.*, 2006, **103**, 10186–10191.
2 T. D. Bennett and S. Horike, *Nat. Rev. Mater.*, 2018, **3**, 431–440.
3 B. Chen, Z. Yang, Y. Zhu and Y. Xia, *J. Mater. Chem. A*, 2014, **2**, 16811–16831.
4 B. R. Pimentel, A. Parulkar, E. K. Zhou, N. A. Brunelli and R. P. Lively, *ChemSusChem*, 2014, **7**, 3202–3240.
5 H. Furukawa, K. E. Cordova, M. O'Keeffe and O. M. Yaghi, *Science*, 2013, **341**, 1230444.
6 M. Safaei, M. M. Foroughi, N. Ebrahimpoor, S. Omidi, A. Jahani and M. Khatami, *TrAC, Trends Anal. Chem.*, 2019, **118**, 401–425.
7 M. I. Nandasiri, S. R. Jambovane, B. P. McGrail, H. T. Schaef and S. K. Nune, *Coord. Chem. Rev.*, 2016, **311**, 38–52.
8 Y. Wang, H. Jin, Q. Ma, K. Mo, H. Mao, A. Feldhoff, X. Cao, Y. Li, F. Pan and Z. Jiang, *Angew. Chem., Int. Ed.*, 2020, **59**, 4365–4369.
9 A. Kertik, L. H. Wee, K. Sentosun, J. A. R. Navarro, S. Bals, J. A. Martens and I. F. J. Vankelecom, *ACS Appl. Mater. Interfaces*, 2020, **12**, 2952–2961.
10 H. T. Kwon and H. K. Jeong, *J. Am. Chem. Soc.*, 2013, **135**, 10763–10768.
11 T. D. Bennett, J. C. Tan, Y. Yue, E. Baxter, C. Ducati, N. J. Terrill, H. H. M. Yeung, Z. Zhou, W. Chen, S. Henke, A. K. Cheetham and G. N. Greaves, *Nat. Commun.*, 2015, **6**, 1–7.
12 A. Qiao, T. D. Bennett, H. Tao, A. Krajnc, G. Mali, C. M. Doherty, A. W. Thornton, J. C. Mauro, G. N. Greaves and Y. Yue, *Sci. Adv.*, 2018, **4**, eaao6827.
13 C. Zhou, L. Longley, A. Krajnc, G. J. Smales, A. Qiao, I. Erucar, C. M. Doherty, A. W. Thornton, A. J. Hill, C. W. Ashling, O. T. Qazvini, S. J. Lee, P. A. Chater, N. J. Terrill, A. J. Smith, Y. Yue, G. Mali, D. A. Keen, S. G. Telfer and T. D. Bennett, *Nat. Commun.*, 2018, **9**, 1–9.

14 R. S. K. Madsen, A. Qiao, J. Sen, I. Hung, K. Chen, Z. Gan, S. Sen and Y. Yue, *Science*, 2020, **367**, 1473–1476.
15 A. Qiao, H. Tao, M. P. Carson, S. W. Aldrich, L. M. Thirion, T. D. Bennett, J. C. Mauro and Y. Yue, *Opt. Lett.*, 2019, **44**, 1623.
16 T. To, S. S. Sørensen, M. Stepniewska, A. Qiao, L. R. Jensen, M. Bauchy, Y. Yue and M. M. Smedskjaer, *Nat. Commun.*, 2020, **11**, 2593.
17 M. Stepniewska, K. Januchta, C. Zhou, A. Qiao, M. M. Smedskjaer and Y. Yue, *Proc. Natl. Acad. Sci. U. S. A.*, 2020, **117**, 10149–10154.
18 L. Frentzel-Beyme, M. Kloß, R. Pallach, S. Salamon, H. Moldenhauer, J. Landers, H. Wende, J. Debus and S. Henke, *J. Mater. Chem. A*, 2019, **7**, 985–990.
19 P. Krokidas, S. Moncho, E. N. Brothers, M. Castier and I. G. Economou, *Phys. Chem. Chem. Phys.*, 2018, **20**, 4879–4892.
20 R. R. Kuruppathparambil, R. Babu, H. M. Jeong, G. Y. Hwang, G. S. Jeong, M. Kim, D. W. Kim and D. W. Park, *Green Chem.*, 2016, **18**, 6349–6356.
21 G. Kaur, R. K. Rai, D. Tyagi, X. Yao, P. Z. Li, X. C. Yang, Y. Zhao, Q. Xu and S. K. Singh, *J. Mater. Chem. A*, 2016, **4**, 14932–14938.
22 A. M. Bumstead, M. F. Thorne and T. D. Bennett, *Faraday Discuss.*, 2021, **225**, 210–225.
23 M. A. Ali, J. Ren, T. Zhao, X. Liu, Y. Hua and Y. Yue, *ACS Omega*, 2019, **4**, 12081–12087.
24 F.-X. Coudert and A. H. Fuchs, *Coord. Chem. Rev.*, 2016, **307**, 211–236.
25 R. B. Getman, Y.-S. Bae, C. E. Wilmer and R. Snurr, *Chem. Rev.*, 2011, **112**, 703–723.
26 J.-C. Tan, B. Civalleri, C.-C. Lin, L. Valenzano, R. Galvelis, P.-F. Chen, T. D. Bennett, C. Mellot-Draznieks, C. M. Zicovich-Wilson and A. K. Cheetham, *Phys. Rev. Lett.*, 2012, **108**, 095502.
27 A. U. Ortiz, A. Boutin, A. H. Fuchs and F.-X. Coudert, *Phys. Rev. Lett.*, 2012, **109**, 195502.
28 J. C. Tan, T. D. Bennett and A. K. Cheetham, *Proc. Natl. Acad. Sci. U. S. A.*, 2010, **107**, 9938–9943.
29 A. M. Walker, B. Civalleri, B. Slater, C. Mellot-Draznieks, F. Corà, C. M. Zicovich-Wilson, G. Román-Pérez, J. M. Soler and J. D. Gale, *Angew. Chem., Int. Ed.*, 2010, **49**, 7501–7503.
30 M. Gao, A. J. Misquitta, L. H. Rimmer and M. T. Dove, *Dalton Trans.*, 2016, **45**, 4289–4302.
31 P. G. Boyd, S. M. Moosavi, M. Witman and B. Smit, *J. Phys. Chem. Lett.*, 2017, **8**, 357–363.
32 R. Gaillac, P. Pullumbi, K. A. Beyer, K. W. Chapman, D. A. Keen, T. D. Bennett and F.-X. Coudert, *Nat. Mater.*, 2017, **16**, 1149–1155.
33 L. Zhang, Z. Hu and J. Jiang, *J. Am. Chem. Soc.*, 2013, **135**, 3722–3728.
34 Z. Hu, Y. Chen and J. Jiang, *J. Chem. Phys.*, 2011, **134**, 134705.
35 Y. Yang, Y. K. Shin, S. Li, T. D. Bennett, A. C. T. van Duin and J. C. Mauro, *J. Phys. Chem. B*, 2018, **122**, 9616–9624.
36 Y. Yang, C. J. Wilkinson, K.-H. Lee, K. Doss, T. D. Bennett, Y. K. Shin, A. C. T. van Duin and J. C. Mauro, *J. Phys. Chem. Lett.*, 2018, **9**, 6985–6990.
37 D. Dubbeldam, K. S. Walton, D. E. Ellis and R. Q. Snurr, *Angew. Chem., Int. Ed.*, 2007, **46**, 4496–4499.
38 A. Bax, *J. Magn. Reson.*, 1985, **65**, 142–145.
39 S. Grimme, J. Antony, S. Ehrlich and H. Krieg, *J. Chem. Phys.*, 2010, **132**, 154104.
40 F. Birch, *Phys. Rev.*, 1947, **71**, 809.
41 S. Plimpton, *J. Comput. Phys.*, 1995, **117**, 1–19.
42 M. A. Addicoat, N. Vankova, I. F. Akter and T. Heine, *J. Chem. Theory Comput.*, 2014, **10**, 880–891.
43 D. E. Coupry, M. A. Addicoat and T. Heine, *J. Chem. Theory Comput.*, 2016, **12**, 5215–5225.
44 A. K. Rappé, C. J. Casewit, K. S. Colwell, W. A. Goddard III and W. M. Skiff, *J. Am. Chem. Soc.*, 1992, **114**, 10024–10035.
45 L. Vanduyfhuys, S. Vandenbrande, J. Wieme, M. Waroquier, T. Verstraelen and V. van Speybroeck, *J. Comput. Chem.*, 2018, **39**, 999–1011.
46 T. D. Bennett, Y. Yue, P. Li, A. Qiao, H. Tao, N. G. Greaves, T. Richards, G. I. Lampronti, S. A. T. Redfern, F. Blanc, O. K. Farha, J. T. Hupp, A. K. Cheetham and D. A. Keen, *J. Am. Chem. Soc.*, 2016, **138**, 3484–3492.
47 P. Krokidas, M. Castier, S. Moncho, E. Brothers and I. G. Economou, *J. Phys. Chem. C*, 2015, **119**, 27028–27037.
48 S. Henke, M. T. Wharmby, G. Kieslich, I. Hante, A. Schneemann, Y. Wu, D. Daisenberger and A. K. Cheetham, *Chem. Sci.*, 2018, **9**, 1654–1660.
49 K. Li, Z. Ding and D. Xue, *Funct. Mater. Lett.*, 2010, **3**, 241–244.
50 I. D. Brown, P. Klages and A. Skowron, *Acta Crystallogr., Sect. B: Struct. Sci.*, 2003, **59**, 439–448.
51 P. Z. Moghadam, A. Li, S. B. Wiggin, A. Tao, A. G. P. Maloney, P. A. Wood, S. C. Ward and D. Fairen-Jimenez, *Chem. Mater.*, 2017, **29**, 2618–2625.
52 L. Chen, T. Mashimo, C. Iwamoto, H. Okudera, E. Omurzak, H. S. Ganapathy, H. Ihara, J. Zhang, Z. Abdullaeva, S. Takebe and A. Yoshiasa, *Nanotechnology*, 2013, **24**, 045602.
53 J. Kjeldsen, M. M. Smedskjaer, J. C. Mauro and Y. Yue, *J. Non-Cryst. Solids*, 2014, **406**, 22–26.
54 J. Kjeldsen, M. M. Smedskjaer, J. C. Mauro and Y. Yue, *Appl. Phys. Lett.*, 2014, **104**, 051913.
55 F. A. Lindemann, *Phys. Z.*, 1910, **11**, 609–612.
56 D. Radhakrishnan and C. Narayana, *J. Chem. Phys.*, 2015, **143**, 234703.
57 G. Khandelwal, N. P. Maria Joseph Raj and S. J. Kim, *J. Mater. Chem. A*, 2020, **8**, 17817–17825.
58 *NIST Chemistry WebBook*, NIST Standard Reference Database Number 69, ed. P. J. Linstrom and W. G. Mallard, National Institute of Standards and Technology, Gaithersburg MD, 2005, p. 20899, http://webbook.nist.gov, accessed August 2021.